water

MDPI

Article

On the Relationship of Arctic Oscillation with Atmospheric Rivers and Snowpack in the Western United States Using Long-Term Multi-Platform Dataset

Samuel Liner [1], Ju-Mee Ryoo [2,3] and Sen Chiao [4,*]

[1] Department of Meteorology and Climate Science, San José State University, San Jose, CA 95192, USA; samuel.liner@sjsu.edu
[2] Earth Science Division, NASA Ames Research Center, Mountain View, CA 94035, USA; ju-mee.ryoo@nasa.gov
[3] Science and Technology Corporation, Mountain View, CA 94035, USA
[4] NOAA Cooperative Science Center in Atmospheric Sciences and Meteorology (NCAS-M), Howard University, Washington, DC 20059, USA
* Correspondence: sen.chiao@howard.edu

Abstract: Atmospheric rivers (ARs) are narrow bands of enhanced integrated water vapor transport, modulated by large-scale and synoptic-scale variability. Here, we investigate how ARs and snowpack are shaped by large-scale variability such as arctic oscillation (AO) by examining the synoptic conditions and characteristics of ARs and snowpack in the different phases of AO. Using Integrated Multi-Satellite Retrievals for Global Precipitation Measurement (IMERG) data, Modern-Era Retrospective analysis for Research and Applications, Version 2 (MERRA2) reanalysis data, and in-situ observation data over the eastern Pacific and western United States. we found that more precipitation is observed in lower latitudes (35° N–45° N) during negative AO months and farther north (north of 45° N) in latitude during positive AO months. These are associated with wavelike synoptic patterns in negative AO months and more straight-line type synoptic patterns in positive AO months. The different phases of AO also modulate the AR characteristics: 2.6% less intense (5.3% more intense) integrated water vapor transport and total precipitation, and 16.0% shorter (21.1% longer) duration of ARs than the climatological mean (1980–2019) for positive AO (negative AO) phase. AR frequency is also higher (~50.4%) than the climatological mean for negative AO phase, but there is no statistically significant difference between either negative AO or positive AO phase, especially in southern California. In addition, the snow water equivalent (SWE) tends to be reduced in the positive AO phase and under high-temperature conditions, especially in recent years (2010s). The similar relationships are found in the early 1990s and 2000s, but their statistical significances are low. Considering that lower atmospheric temperature keeps increasing over the eastern Pacific and the western U.S., and SWE tends to be reduced in the positive AO phase in recent years, SWE may decrease over northern California if the warming condition persists. These findings highlight how the characteristics of local extreme weather can be shaped by large-scale climate variability.

Keywords: atmospheric rivers; arctic oscillation; integrated water vapor transport; snow water equivalent; climate variability

check for updates

Citation: Liner, S.; Ryoo, J.-M.; Chiao, S. On the Relationship of Arctic Oscillation with Atmospheric Rivers and Snowpack in the Western United States Using Long-Term Multi-Platform Dataset. *Water* **2022**, *14*, 2392. https://doi.org/10.3390/w14152392

Academic Editors: Jorge Eiras-Barca and René Garreaud

Received: 15 June 2022
Accepted: 27 July 2022
Published: 2 August 2022

Publisher's Note: MDPI stays neutral with regard to jurisdictional claims in published maps and institutional affiliations.

Copyright: © 2022 by the authors. Licensee MDPI, Basel, Switzerland. This article is an open access article distributed under the terms and conditions of the Creative Commons Attribution (CC BY) license (https://creativecommons.org/licenses/by/4.0/).

1. Introduction

Atmospheric rivers (ARs) are narrow bands of enhanced integrated water vapor transport (IVT), which typically transfer moisture from the tropics and subtropics into the higher midlatitudes [1]. While there are many regional and global AR detection methods [2–6], ARs generally are characterized by the filamentary shape of strong water vapor transport associated with extratropical cyclones and proceeded by a low-level jet stream, categorized by their IVT (typically greater than ~250 kg m^{-1} s^{-1}) and high integrated water vapor (IWV; >2 cm) [7]. The advent of the Special Sensor Microwave Imager (SSM/I), which has

provided extensive integrated water vapor measurements across the globe, has made the characteristics of ARs clearer, especially over the ocean [7]. Furthermore, although ARs only cover about ten percent of the globe longitudinally, they transport up to ninety percent of poleward water vapor [1,8,9].

While ARs occur globally, ARs are particularly important to California's water resources, contributing up to fifty percent of the state's annual precipitation and streamflow [10]. Studies have demonstrated the importance of ARs and snowpack in the Sierra Nevada mountains regarding water resources, drought, and flooding [10–12]. An increased number of ARs can also influence the snowpack. For example, rain-on-snow (ROS) events during ARs, i.e., when precipitation as rain falls onto existing snowpack during ARs, increase flood risks and boost snowmelt [13]. ROS and AR events occurring in different locations can have opposing effects on snowpack, as shown by Goldenson et al. [14], where there was an increase in snowpack in the Sierra Nevada Mountains and a decrease in snowpack in the Cascade Mountain Range. Hence, understanding the AR characteristics and their regional dependency is also critical to accurately estimating the snowpack and monitoring it in the western United States.

The actual contribution of ARs to the rain and snowpack in California depends on where they make landfall, which is often associated with the geographic difference [2,11,15]. Geographical differences of ARs are based on the terrain of the area. Since water vapor transported in ARs is lower than in the atmosphere (under ~700 hPa), it is especially subject to orographic lifting, which is when moist air flows from lower terrain to higher terrain causing the air to cool and form clouds, producing precipitation [11]. From this, it can be concluded that the location of the AR landfall is closely associated with the type of terrain, which in turn influences how much water vapor falls as precipitation and how far inland the AR's influence reaches [15]. Because of this, it has been observed that the number of ARs that reach farther into the interior is highest in the Pacific Northwest, especially over lower elevation areas, while fewer ARs make it over the High Sierra Nevada mountains and into the Great Basin [2]. These features are largely modulated by different atmospheric circulation and conditions from daily to decadal time scales.

Although ARs are largely governed by the regional moisture flux and meteorological conditions, they are also controlled by large-scale climate variability [16,17] with different temporal scales. The climate variability, such as El Niño-Southern Oscillation (ENSO), Arctic Oscillation (AO), Madden-Julian Oscillation (MJO), and Pacific/North American Teleconnection Pattern (PNA), modulates different meteorological conditions that frequently fluctuate, demonstrating their possible linkages to ARs. ENSO strengthens or weakens surface winds [18] over the ocean, which typically enhances the regional difference in precipitation. AO and PNA are associated with changes in atmospheric pressure over the land and the ocean in the Northern Hemisphere (NH). Ryoo et al. [19] showed that U.S. west coast precipitation is highly modulated by the ENSO through the Rossby wave breakings associated with the change in the location and intensity of the subtropical upper-level jet and moisture transport pathways.

Recent studies, however, presented contrasting results. For instance, no significant correlations were found between Sea surface temperature (SST) based El Niño Southern Oscillation and ARs in the Pacific Northwest [17,19] although more frequent AR was observed in positive Southern Oscillation Index (SOI) [17]. In contrast, a significant relationship was found between ENSO and AR activities over the east Asian and northwestern Pacific [20]. Guan et al. [16] also reported that the high frequency of ARs over California is favored by the negative phase of the Arctic Oscillation (AO) and Pacific-North American (PNA) teleconnection patterns. While the negative AO tends to bring more precipitation in California [16] and cause more extreme precipitation when combined with the positive SOI [17], positive AO was also shown to increase wintertime precipitation in high latitude regions [21]. More recently, using a self-organizing map, Kim and Chiang [22] separated the various climate modes into two groups based on their synoptic variabilities, such as the ENSO mode and jet mode (including the AO index), and showed that these synoptic

patterns are closely associated with the distinct AR characteristics such as genesis, landfall location, and duration. However, this study also relied on the reanalysis product and surface observation, and the use of satellite or in-situ data over a long period of record has not been presented.

The primary goal of this paper is to understand further how the AR characteristics, local precipitation, and snowpack vary with large-scale climate variability. The specific science objectives to determine are (1) the synoptic conditions shaped by the different phases of AO, (2) how the different phases of the large-scale AO patterns impact the characteristics of ARs in terms of intensity, duration, and frequency, and (3) how they are related to local precipitation, snowpack, and other climate factors such as temperature and stability over the different regions in the western U.S. To address these objectives, we use long records of the 3-hourly (1980–2019) and monthly (1980–2020) MERRA2 reanalysis data combined with the monthly IMERG satellite data (2001–2019) to extensively investigate how the different phases of AO are associated with regional precipitation patterns and how they are coupled to the synoptic conditions that favor ARs over the western U.S. The example of AR captured in IMERG precipitation data is shown along with the region of focus in this study in Figure 2.

We describe the data and methods in Section 2. The dominant synoptic patterns during the different phases of AO and associated AR characteristics and snowpack are examined in Section 3. In Section 4, the discussion and conclusions of this study are provided.

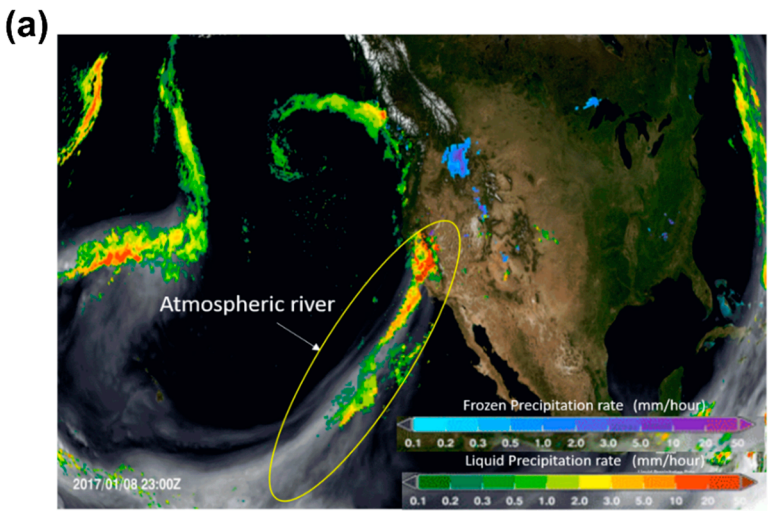

Figure 1. *Cont.*

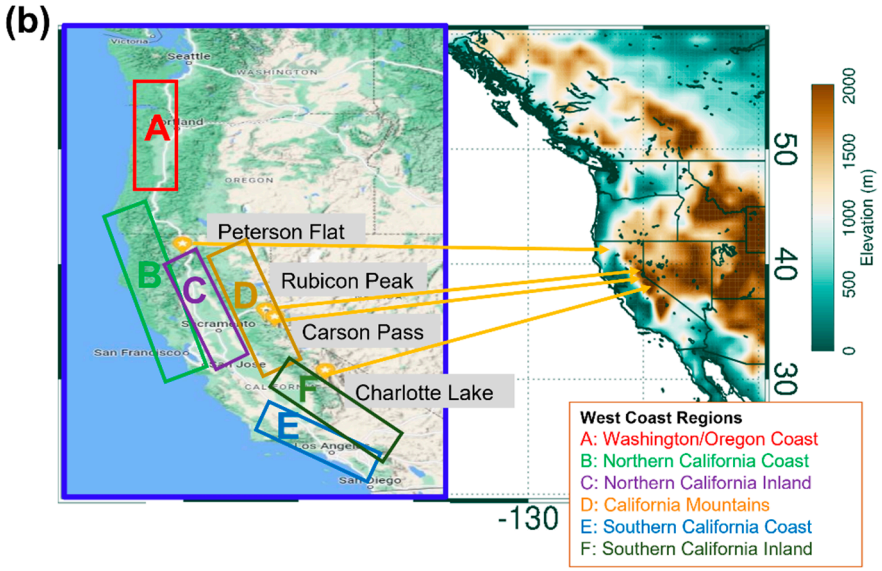

Figure 2. (**a**) The example of GPM precipitation for the 8 January 2017 AR event, striking the western U.S (figure credit: NASA GPM [23]). (**b**) The elevation map of the western U.S. and snowpack site (Peterson Flat (41.3° N, 122.5° W), Rubicon Peak (39.0° N, 120.1° W, Carson Pass (38.7° N, 120.0° W), and Charlotte Lake (36.8° N, 118.4° W)) in the western U.S. The blue box refers to the AR characteristic study (A–F) region and snowpack observation sites (yellow dot and arrows).

2. Data and Methods

2.1. Data

We utilized a long-term multiplatform dataset including reanalysis, satellite, and local observation. Our study regions cover the eastern Pacific and western U.S; for regional AR and SWE analysis, we focus on the local sites, but for synoptic scale analysis, we include the eastern Pacific and the western U.S. (160–100° W, 30–50° N). The study period spans the whole months of the year, but we focused on October through April for synoptic structure and AR characteristic analysis because precipitation and moisture transport associated with dynamic processes over the western U.S. is most active during that period. The individual dataset we used in this study are described in the following subsections.

2.1.1. MERRA2

Meteorological variables analyzed in this study were collected from NASA's Modern-Era Retrospective analysis for Research and Applications version 2 (MERRA2) [24,25], including sea level pressure (SLP), geopotential height at 1000 hPa and 500 hPa, air temperature at 850 hPa, horizontal wind (u, v) at 850, 500, and 250 hPa, potential temperature at 700 hPa and 1000 hPa, and vertically integrated water vapor flux. Both instantaneous 3-dimensional and time-averaged 2-dimensional 3-hourly [26] and monthly mean [27,28] data collections were implemented with a spatial resolution of 0.5° × 0.625°. Produced by the Global Modeling and Assimilation Office (GMAO) of NASA, MERRA2 uses the Goddard Earth Observing System Model (GEOS) version 5.12.4 and covers the period from 1980 onward.

A recent AR study showed that enhanced integrated water vapor transport in MERRA-2 leads to increased AR detection with fixed thresholds relative to JRA-55 and ERA5 [29]. A comparison study of the reanalyses with dropsonde data showed that IVT error is lowest in ERA-5 [30]. However, their overall patterns of IVT are comparable, although the absolute value of IVT differs among reanalyses [29], potentially indicating the uncertainty of the use of MERRA2 data on AR characteristics associated with the different phases of AO is expected to be small.

For AR characteristic analysis, the integrated water vapor transport (IVT), calculated in kilograms per meter per second, was used. This is key in determining atmospheric rivers'

strength and precipitation outcome [31]. The IVT data were initially measured from the MERRA2 reanalysis product and then collated into an AR catalog [2]. IVT was calculated using the following formula:

$$IVT = \frac{1}{g}\int_{P_{sfc}}^{100\ \text{hPa}} qV\,dp \quad (1)$$

where p_{sfc} is the pressure at the surface, q is the specific humidity, V is the total horizontal wind vector, and g is the gravitational acceleration [2]. We collected IVT data from five sites spanning the six different subregions, each represented by a northern point, a central point, and a southern point, to obtain a large-scale average to best facilitate the AO impact on the regional scale ARs. The data were originally available at a 3-hourly resolution and later averaged into monthly data for time series analysis for ARs. Additional data from this database were AR duration and the total number of AR occurrences (referred to AR frequency).

2.1.2. Integrated Multi-Satellite Retrievals for Global Precipitation Measurement (IMERG)

Global precipitation data were acquired from NASA's Integrated Multi-satellite Retrievals for GPM (IMERG) with daily and monthly resolution as a level 3 final run product [32]. IMERG data fuse the TRMM era (2000–2015) precipitation estimates with GPM era (2014–present) precipitation estimates by combining all satellite microwave precipitation estimates with microwave-calibrated infrared (IR) satellite estimates. IMERG data were collected from the first full year after inception in 2001 through 2019 and had a monthly timescale resolution and a 0.1° by 0.1° spatial resolution up to ~60° S and 60° N. The monthly anomalies were calculated by subtracting the seasonal mean from the data.

It has been reported that the IMERG products tend to underestimate the orographic precipitation compared to the rain gauge data and can be sensitive to the number of available gauges used for the calibration process of IMERG [33,34]. While there is a good agreement between IMERG and CLoudSat for precipitation in extratropical cyclones [35], the IMERG product has uncertainty in terms of the precipitation rates; it is reported to show greater precipitation rates than CloudSat [35] in moist environments and lower precipitation rates in dry and moderately moist environments [36] and vigorously ascending regions associated with the extratropical cyclones [37].

Despite this limitation, the IMERG product has been tested and proven to be (i) generally good at a regional scale [38], (ii) more accurate than the GPM core mission precipitation product [39], and (iii) known to be better suited to track cyclones than the daily Global Precipitation Climatology Project dataset [40]. Thus, with these uncertainties in mind, the IMERG final products formed an adequate dataset for understanding the precipitation features and characteristics associated with an AR, which is a part of extratropical cyclones and is affected by the synoptic- and large-scale variability on a global and regional scale in the western U.S.

2.1.3. Arctic Oscillation (AO), Snow Water Equivalent (SWE), Rain-On-Snow (ROS), and Local Land Precipitation

The Arctic Oscillation (AO) index is a measurement of 1000 hPa geopotential height anomalies north of 20° N [41]. These data were collected from the National Weather Service's Climate Prediction Center [41]. The index is measured daily and was collected as a monthly average when examining 40 years. To filter out such large fluctuating patterns, we calculated the three-month running average for time series analysis (Figure 3).

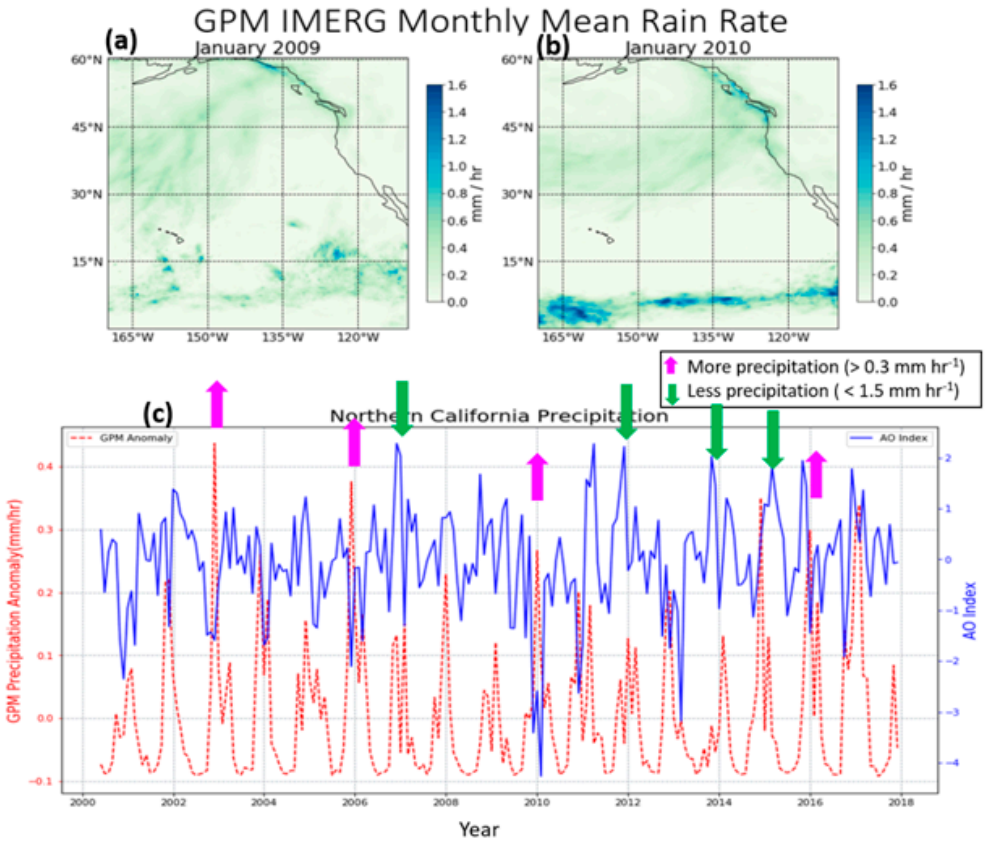

Figure 3. IMERG Precipitation during (**a**) January 2009 and (**b**) January 2010. (**a**,**b**) correspond to positive AO months and negative AO months, respectively. (**c**) Time series of monthly GPM precipitation and AO index. Precipitation data were calculated by taking the average over the entire northern CA area [122–124° W and 36.5–42° N].

Data used to analyze snow accumulation and corresponding total precipitation were gathered from the California Data Exchange Center provided by the California Department of Water Resources from 1985 to 2020 [42]. The data were originally available in hourly resolution but later averaged into monthly data to associate them with AO index and other meteorological variables. Since this database mainly covers the state of California, the time and spatial aspects of our data were limited by this. In addition, since the quality of the reanalysis data in the mountain or near-surface regions is poor or unavailable [43], surrounding air temperature measurements were used in this SWE analysis and were collected from the same local sites. We also used these measurements to determine ROS events, which are defined when the SWE decreased while the total precipitation increased.

2.2. Methodology

Percentage Difference, Anomaly Calculation, and Correlation Analysis

The behavior of ARs can vary greatly based on locations [15,44]. Thus, to better understand how positive and negative AO months differ from the climatological mean (1980–2019) in different sectors of the western U.S., we calculated the percentage difference for each analyzed month, especially for AR characteristic analysis. The percentage difference is computed by subtracting the average of all months from the average of positive or negative AO months and dividing by the average of all months. For those analyses, we calculated the average for AO months greater than +1.5 (less than −1.5) for the positive (negative) AO phases, respectively. The formula used to calculate these differences was as follows:

$$A\% = \frac{(m_a - c_a) \times 100}{c_a} \quad (2)$$

where m_a is the average of the analyzed month and c_a is the climatological mean of that month.

We also calculated the anomaly of the variables to discern how different the given month or periods are compared to the climatological mean. Each anomaly field was computed by subtracting the climatological monthly mean value from each monthly mean value. The correlation analysis was performed to determine the correlation among variables. The student's *t*-test was used to determine if there was a significant difference between the two groups mean and to obtain the statistical significance.

3. Results

Figure 3 shows the example of precipitation of January 2009 and 2010 corresponding to a negative and positive AO index, along with the time series of the IMERG precipitation anomaly from the climatological mean (2001–2019) overlaid by the AO monthly index. Although there is large month-to-month precipitation variability, we see some noteworthy areas indicating a possible linkage between precipitation and AO.

For example, high precipitation is observed over the northeastern Pacific and north of the western U.S. in positive AO months (e.g., January 2009), while a high precipitation rate is found in the lower latitudes such as Washington, Oregon, and northern California in negative AO months (e.g., January 2010), when AO is in the opposite phase. Interestingly, the AO index tends to have a negative phase for the higher precipitation events during 2003, 2006, 2010, and 2016. In contrast, the AO index tends to be highly positive or marginally positive for the lower precipitation events during 2007, 2012, 2014, and 2015. This suggests that large-scale climate variability such as AO can modulate local precipitation. The detailed characteristics will be discussed in the following sections.

3.1. Synoptic Characteristics of ARs in Different Phases of AO

3.1.1. Examples of SLP and Wind Features in Different Phases of AO

Since synoptic conditions can be affected by the different phases of AO, we first examined synoptic conditions associated with different phases of AO. Dates of the AO phase from all months greater than +1.5 (less than −1.5) from 1980 to 2019 were gathered (not shown) and were referred as top positive AO (negative AO) months. From this, we classified the top positive AO and top negative AO months and then compared the top positive and negative AO months to the whole 40-year span. Figure 4a,c show the distinct SLP patterns in the different phases of AO from the top positive and negative AO months.

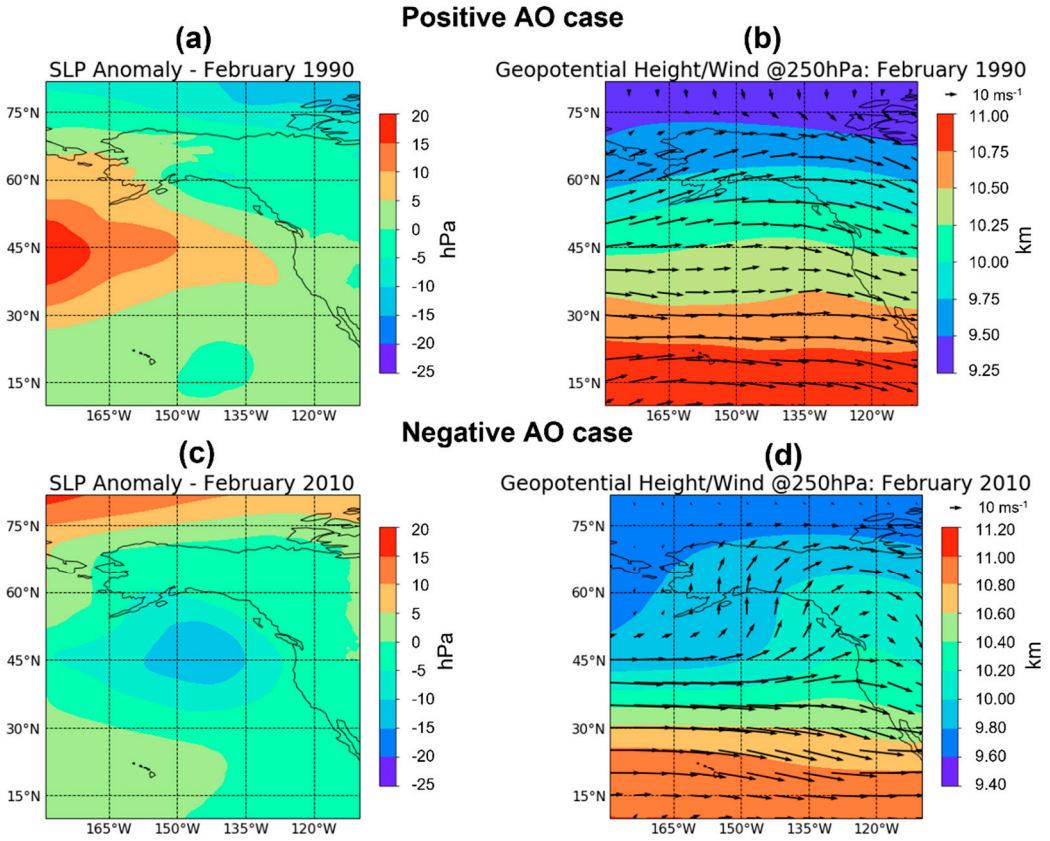

Figure 4. Longitude-latitude cross-section of (**a**,**c**) sea level pressure (SLP) anomaly and (**b**,**d**) 250 hPa geopotential height and horizontal wind for top positive (>+1.5) and top negative (<−1.5) AO months. The anomaly is computed by subtracting the climatological February mean (1980–2019) from the given negative and positive AO February monthly mean value.

Although there is substantial month-to-month variability, the positive phase tends to have high-pressure systems centered in the northeastern Pacific off the coast of Alaska with lower-than-average SLP over the Arctic. Negative AO months tend to show the opposite pattern with low-pressure systems centered in the eastern Pacific Ocean and higher-than-average pressure in the Arctic region; these patterns are consistent with the previous understanding of AO-pressure-temperature coupling in the Arctic and mid-latitude regions [45,46]. These patterns may prevent cold Arctic flow from moving southward in the positive AO months compared to negative AO months. Similar features associated with a different phase of AO are found in other months and years (not shown).

3.1.2. Composites of SLP, Wind Speed, and Vertically Integrated Water Vapor Flux

To corroborate the different characteristics of synoptic conditions during the different phases of AO, composite analysis was performed on SLP, wind, and vertically integrated zonal water vapor flux for all positive AO months and all negative AO months, shown in Figure 5. The composite of major negative AO months (Figure 4c) confirms the SLP pattern seen in the top negative AO months, i.e., lower SLP off the coast of Alaska and high SLP in the Arctic.

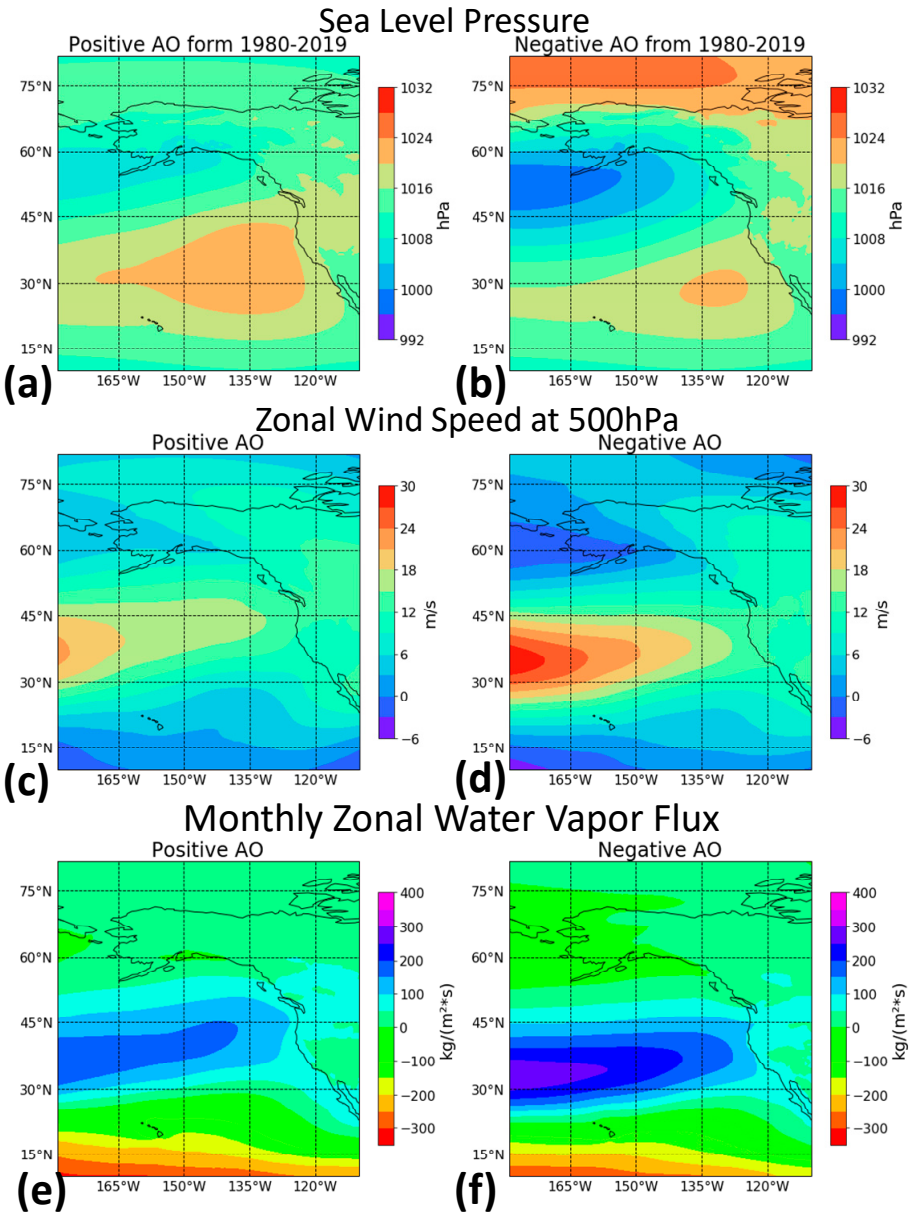

Figure 5. Composite (**a**,**b**) SLP, (**c**,**d**) 500 hPa zonal wind speed, and (**e**,**f**) vertically integrated zonal water vapor flux of all top positive (>+1.5) and top negative (<−1.5) AO months from October through April during 1980–2019.

The two notable things in the negative AO months plot are a lower low-pressure system in the Northeast Pacific and a much higher high-pressure system in the Arctic as compared to the positive AO months. This confirms the pattern shown in the SLP differences during AO phases [45]. It also indicates there can be more meridional flow developing associated with the low-pressure system during the negative phase. Additionally, in the positive months, more ridge-like patterns develop, which can form a warm, high-pressure system over the western U.S., while more trough-like patterns develop in the negative AO months, which can facilitate northward tropical moisture, potentially fueling ARs over the western U.S. (see Figure 4b,d).

The horizontal zonal wind speeds for the positive and negative AO months are shown in Figure 5c,d. These wind maps show that in the negative AO phase, there are strong areas of westerly and easterly winds in the 35° N and 60° N regions, respectively, at all three levels (not shown) that are closer to the North American coast than in the positive AO months. Here, we see opposing patterns in the positive and negative phases of AO, where

there is an area band to the west of the California coast that has lower wind speeds during the positive phase and higher wind speeds during the negative phase (Figure 5c,d). We also found that the low-level jet, often defined as a maximum wind speed (around 12 m s^{-1} or greater) in the lower troposphere [47], plays a critical role in transporting moisture during ARs and occurs more favorably during negative AO phases (not shown). This indicates conditions in negative AO phases may provide favorable conditions for more intense ARs over the western U.S., consistent with the result presented by Guan et al. [16]. We also see a stronger upper-level jet influence on low-level, and therefore AR, moisture transport [48]. From Figure 5c,d, we find a greater eastward air movement in the region that is highly associated with landfalling ARs on the U.S. west coast, with a stronger wind gradient in the negative AO over the eastern Pacific.

Together with the winds at different vertical levels, we also examined the vertically integrated zonal water vapor flux during the positive and negative phases of AO, shown in Figure 5e,f. Enhanced zonal water vapor flux is shown in the negative AO months relative to the positive AO months. Figure 5 suggests that the synoptic conditions indispensable for AR formation, such as a strong low-level jet with high moisture and strong vapor flux, are pronounced during the negative phase of AO over the northwestern U.S. in NH wet seasons.

3.2. Different AR Characteristics during the Different Phases of AO

AR Intensity, Duration, and Frequency

To examine how the different phases of AO are related to AR characteristics such as intensity, duration, and frequency at local scales, we analyzed different regions over the west coast of the U.S., shown in Figure 6a. In this section, we employed the AR data catalog mentioned in Section 2.1.1 to observe any differences between positive and negative AO months compared to all months in the period of 40 years (1980–2019). The six sub-regions, such as (A) Washington/Oregon coast, (B) northern California coast, (C) northern California inland, (D) California mountains, (E) southern California coast, and (F) southern California inland, were chosen from across the western U.S. to observe any differences between the regions (see Figure 6a).

The IVT was averaged for all AR events (when the IVT was greater than 250 kg m^{-1} s^{-1}) during all the positive AO months, and we found the percentage difference from all AR events in that same period, shown in Figure 6b. A similar method was applied to data for all negative AO months in Figure 6c. Notably, the IVT is lower during the positive phase of AO and higher during the negative phase months for almost all regions. Here we define AR intensity as the magnitude of IVT values. Taking the averages for all 30 sites (5 sites for each 6 subregion) during wet months (October through April) over 40 years yields a difference of 2.6% less intense (5.3% more intense) than the climatological mean (1980–2019) for the positive (negative) AO months, significant at the 85% (99%) confidence level.

Figure 6d,e shows the duration difference of each new AR event during the different phases of AO. Like the AR intensity plots (Figure 6b,c), there is a characteristic feature: shorter durations compared to all months during the positive AO phase and longer durations during the negative AO phase in most locations. The overall mean difference for each phase is 16.0% shorter (21.1% longer) than the climatological mean for the positive phase (negative phase) at the 99% confidence level.

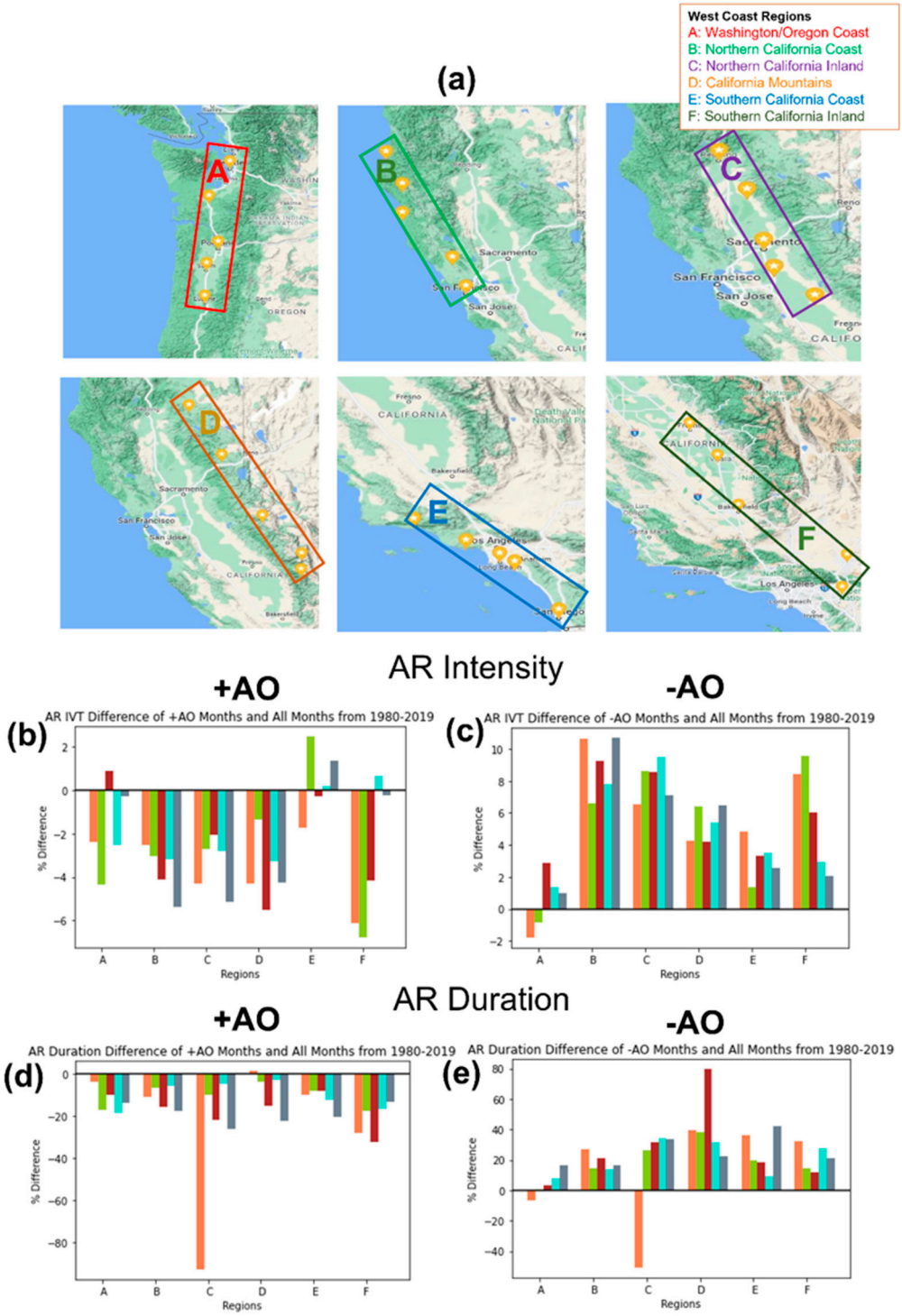

Figure 6. (**Top**) Map of study regions created using Google Maps© (**a**). (**Bottom**) Percentage difference histograms of (**b**,**c**) AR intensity and (**d**,**e**) AR duration during positive AO months and negative AO months from October through April during 1980–2019. The intensity is determined by the magnitude of IVT values. The different colors in the histogram indicate the values at different sites from the northeast to the southwest (from left to right) for each subregion (A–F). The negative values represent a percentage lower than the climatological mean (1980–2019), and the positive values represent a percentage higher than the climatological mean.

The AR frequency difference in the two phases of AO was also analyzed. The AR frequency tends to be larger in the negative AO phase than the climatological mean, but

regional differences are relatively large (not shown). For example, over the region A–D, AR frequency in the positive AO phase (negative AO phase) is about 2.6% less frequent (50.4% more frequent) than the climatological mean, and this is statistically insignificant (significant at 95% confidence level). However, over region E–F (Southern California), there is no statistically significant difference between either the negative AO phase or the positive AO phase (not shown). Given the three characteristics for the severity of ARs shown in Figure 6, negative AO months tend to favor AR formation, intensity, and longevity compared to positive AO months over most of California's coastal and mountainous regions. However, the relationship between AR frequency and the AO phases is relatively insignificant, especially in southern California.

3.3. SWE Characteristics over Northern California during the Different Phases of AO

3.3.1. SWE and ROS Events in Relation to AO

Regional snowpacks are important water resources in California. It is shown that the snowpack is largely modulated by large-scale variability and environmental factors such as temperature [13]. Here, we examined how AO could modulate regional snowpack through SWE measurements. Figure 7 displays the time series between SWE, AO index, and the temperature at 850 hPa. For the SWE time series shown in both plots of Figure 7, we calculated the monthly anomaly to extract the anomalous features in the given year compared to the climatological mean. In this period from 1985 to 2020 we seea few instances of reduced SWE and both higher temperatures and a higher AO index.

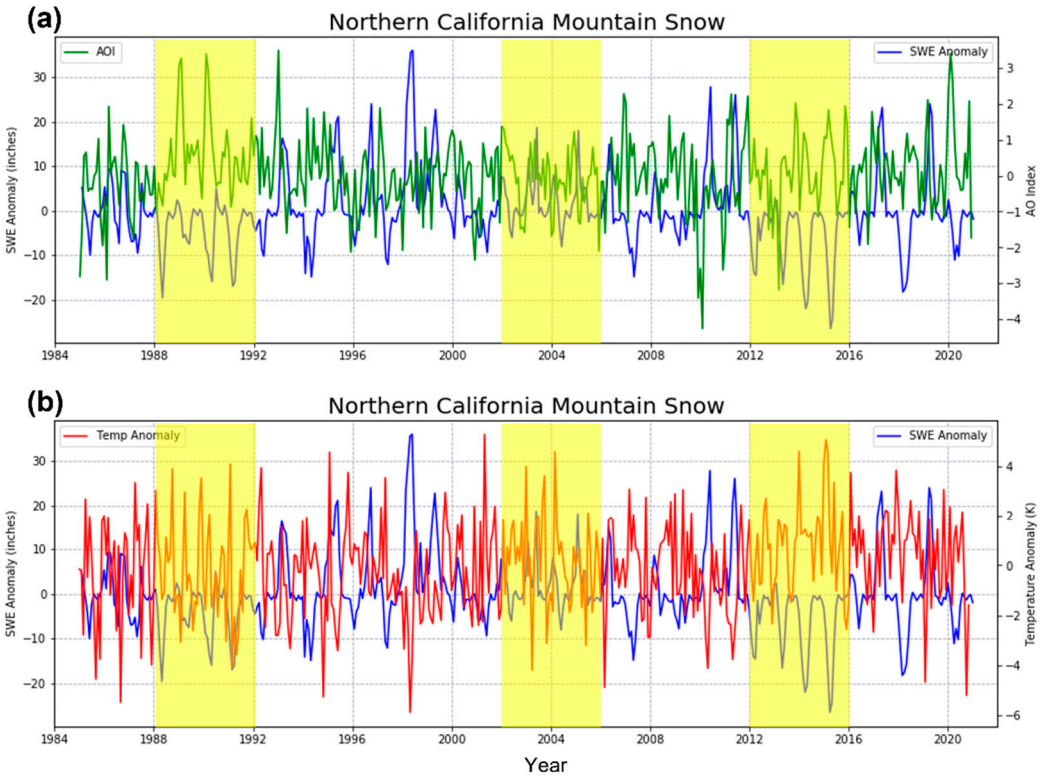

Figure 7. Time series of snow water equivalent (SWE) anomaly in the northern California mountain region (latitude max: 42°, latitude min: 36.8°; longitude max: −120°, longitude min: −124.2°) and the average of the four different sites across the region indicated in Figure 2b, (**a**) the 3-month average AO index and (**b**) 850 hPa air temperature anomaly from 1985 to 2020. The yellow shading refers to the three selective periods of 1988–1992, 2002–2006, and 2012–2016, respectively.

For example, during 2015–2016, a very low SWE anomaly was observed when temperatures warmer than the climatological mean were observed. Sea surface temperature (SST) was also reported to be very high, indicating a strong El Niño and the possible influence

of the El Niño event on AR precipitation during this period [49]. Out of all the months from 1985 to 2020, the positive AO months had 71.4% reduced SWE anomalies compared to all months with 63.7% reduced SWE anomalies and negative AO months with 33.3% reduced SWE anomalies in the northern California mountain regions (see Figure 7). This suggested there also could be an association between ROS events, air temperature, and AO phases because ROS events can occur when the SWE decreases while the total precipitation increases in warmer temperature [13].

The preliminary analysis, however, showed that ROS events are not always linked to the specific phase of AO. Furthermore, the case studies using March 2016 and January 2017 data showed that there is almost the same or insignificant impact of AR and non-AR on ROS (~50%) (not shown), and a similar association was also reported by Guan et al. [13]. Thus, in the following section, we focus on further investigating the association between SWE and AO and their linkages with the recently shifted climate patterns.

3.3.2. Change in SWE in Association with Temperature, SLP, and AO

As mentioned in Section 3.3.1, there was no clear correlation between AO and temperature over a longer period, although there are some strong associations visible in Figure 7 for some periods. Thus, in this section, we aim to look further at the SWE anomaly/AO and SWE anomaly/850 hPa temperature anomaly patterns. Figure 8 shows the correlation plots of the SWE anomaly with the AO and 850 hPa temperature anomaly during three different time periods (1988–1992, 2002–2006, and 2012–2016). They are negatively correlated for all periods (1985–2020) over northern California (not shown), although the significance varies, and the coefficient gets higher in the recent period (Figure 8c).

For example, in the 2012–2016 period, when the warming and drought conditions were persistent, the maximum temperature anomaly was ~5 K greater, and the maximum SWE loss was 25 inches greater than the climatological mean (1985–2020), as shown in Figure 7b. Although the overall relationship between the SWE anomaly and AO index varies by year, a positive AO index tends to be associated with a lower SWE.

This negative correlation accelerated more in the 2010s than in the 1990s as the temperature and SWE anomalies became more positive (not shown). Although the overall significance is lower than that for the few time periods, this shows that recent conditions such as extreme heat, surface warming, and severe drought may enhance the SWE loss in northern California. Indeed, the lower layer mean temperature, represented by the thickness between 500 hPa and 1000 hPa, shows a positive warm anomaly trend that gets more intense in recent years over California and the NH eastern Pacific, as seen in Figure 9.

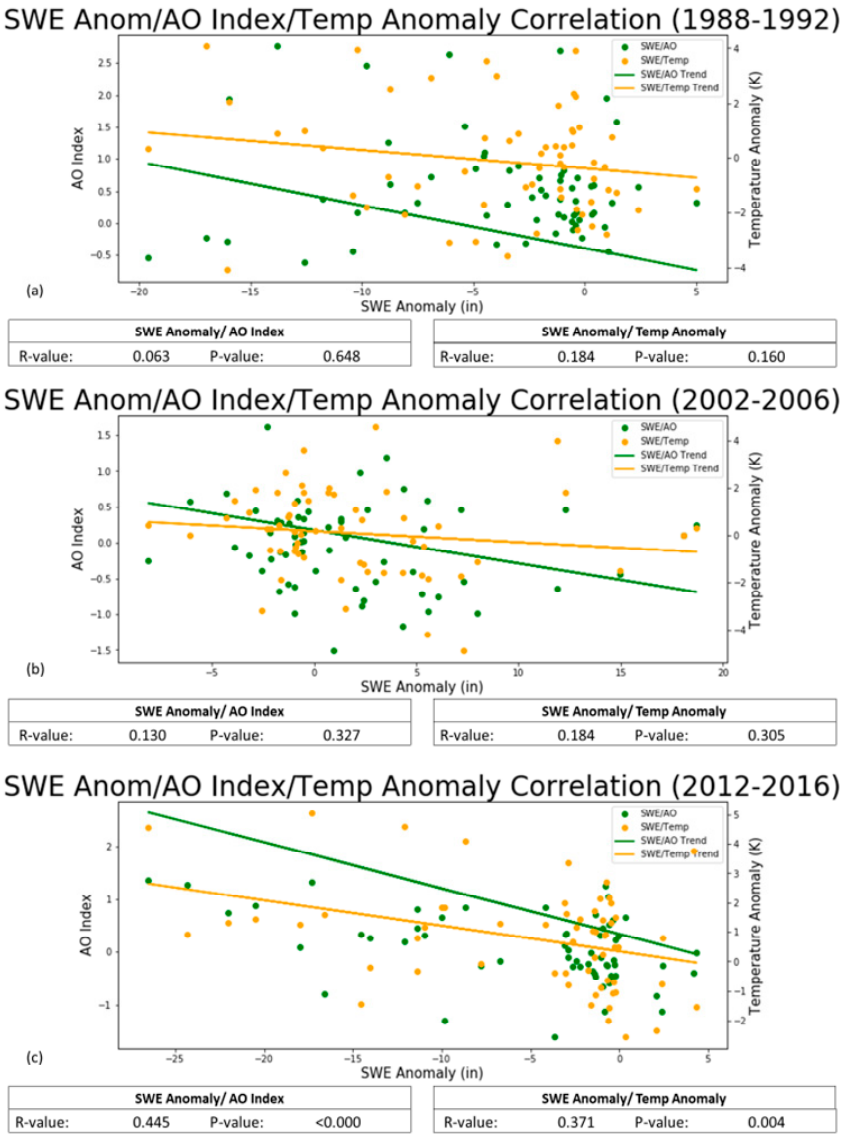

Figure 8. Scatter plot and regression lines for the northern California SWE anomaly as compared to the 3-month average AO index (green) and 850 hPa temperature anomaly (orange) for the three different time periods (1988–1992, 2002–2006, and 2012–2016) highlighted in yellow shadings in Figure 7. The correlation coefficients and their statistical significance for each subplot are provided in the boxes.

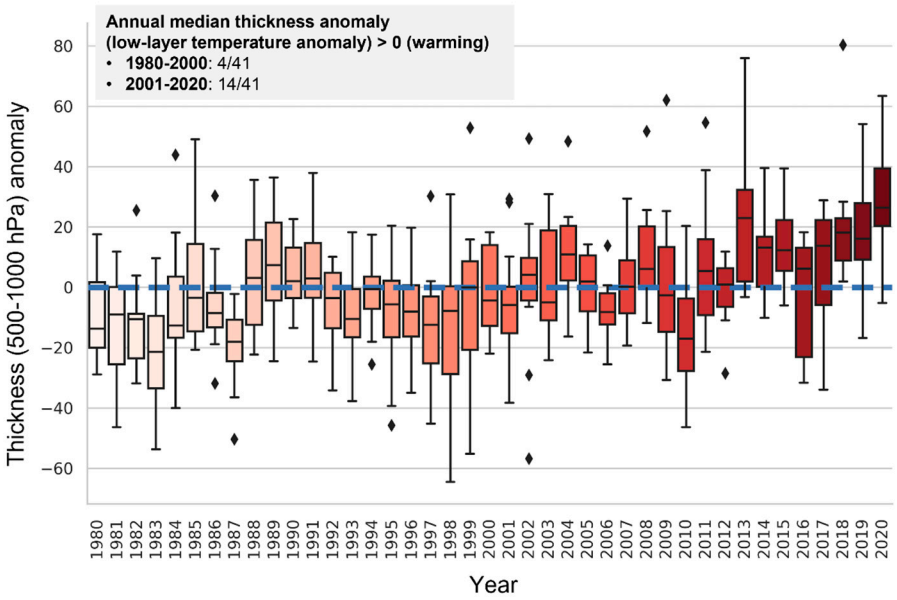

Figure 9. The box-and-whisker plots of the atmospheric layer thickness (500–1000 hPa) anomaly averaged over the eastern Pacific and western U.S. (160–100° W and 30–50° N) from 1980 to 2020 obtained from MERRA2 data. The error bar represents the data within a 95% confidence interval per year. The boxplot's interior line indicates the median for given year; the bottom and top of the boxes are the 25th and 75th percentiles; the upper extreme and the lower extreme whiskers represent the maximum and minimum data. The black dot outside the box indicates the outlier.

The atmospheric variables such as SLP, lower layer mean temperature (i.e., lowermost layer between 500–1000 hPa), and low-level tropospheric stability (LTS; defined by the difference in potential temperature from 700 hPa to 1000 hPa) present interesting relationship, as shown in Figure 10. Clearly shown are: (1) AO index and thickness anomalies tend to be more positive in the recent years with extremes, (2) LTS anomaly increases in recent years (starting from 1998) in a wide range of SLP anomalies (see Figure 10a,b). While the trend of AO is not clearly observed (not shown), AO is positively correlated with the SLP anomaly [R = 0.41, $p < 0.01$] and the LTS anomaly [R = 0.24, $p < 0.01$] (Figure 10a) with the positive AO phase more frequent in recent years (e.g., years after 2008). Considering that SWE tends to be reduced in the positive AO phase and under warmer lower atmospheric temperatures (at 850 hPa; see Figure 8), SWE may decrease over northern California if this warming condition persists. For example, the NH winter of 2019–2020 was an extraordinarily warm year on record in Europe, Asia, and North America with a positive AO phase [50,51], and our analysis indicates that the SWE clearly decreased during that period (see Figure 7). This analysis suggests that AO along with SLP and low-level temperature may be useful metrics to help forecast and predict SWE in northern California.

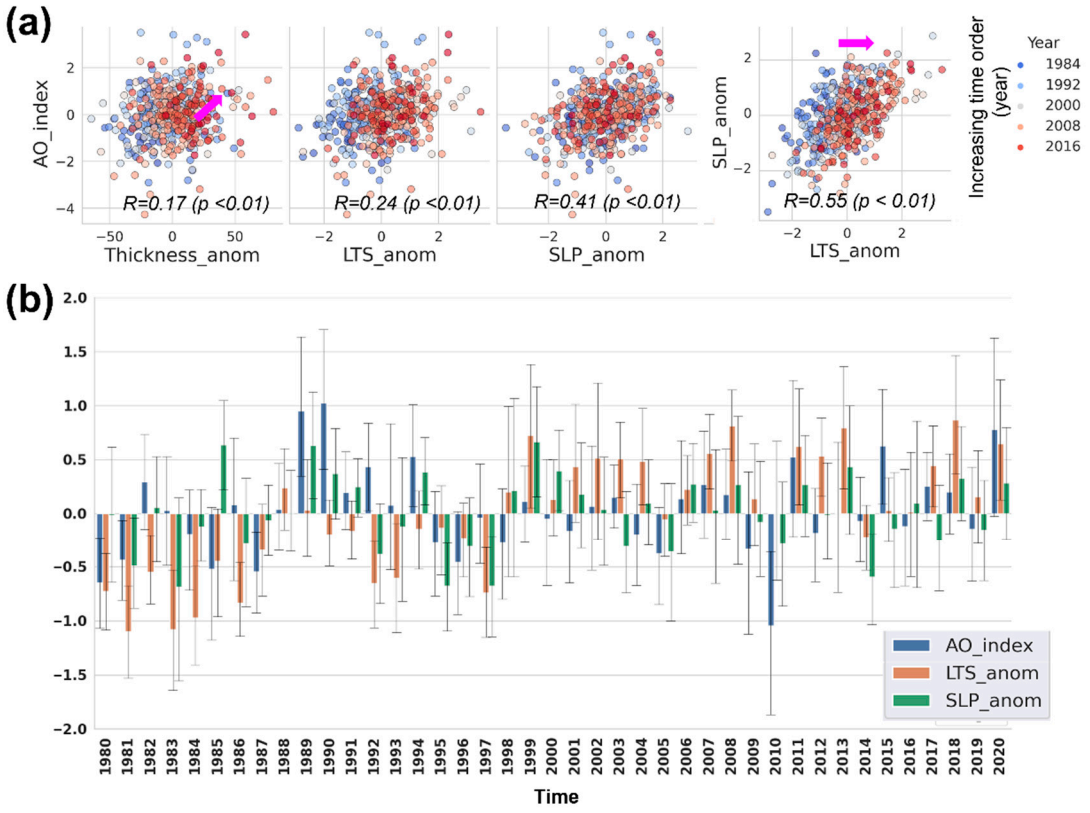

Figure 10. (**a**) (from **left** to **right**) Scatter plots of the AO index with the thickness (geopotential height from 500 to 1000 hPa) anomaly, low-level tropospheric stability (LTS; potential temperature difference between 700 hPa and 1000 hPa) anomaly, and SLP anomaly. Scatter plot of the SLP anomaly with the LTS anomaly. The SLP anomaly is normalized by subtracting the climatological mean from each value and dividing by the standard deviation. The colors of circle markers in (**a**) represent the monthly anomalies of the variables for each year (1980–2020) in increasing time order (from blue to red). (**b**) Time series of the annual mean of AO, LTS anomaly, and SLP anomaly over the eastern Pacific and western U.S. (160–100° W and 30–50° N) from 1980 to 2020. The error bars represent the 95% confidence intervals around the values computed by 5000 bootstrap iterations. The R-value in (**a**) represents the Pearson correlation coefficient at a 99% confidence level. The magenta arrow in (**a**) represents the shifted pattern over time.

4. Discussion and Conclusions

We investigated how the synoptic and large-scale conditions are shaped by the Arctic Oscillation (AO) and how they are associated with different characteristics of atmospheric rivers (ARs) and local snowpack, particularly focusing on the western U.S. We utilized multi-platform dataset including reanalysis, satellite, and local observation from 1980 to 2020, depending on the data availability.

We first demonstrated that the synoptic conditions of the negative phase of AO are associated with the upper-level wavelike patterns in the northern Pacific region with a strong low-level jet, transporting more moisture to the western U.S.. We also showed quantitatively that the negative AO months had more intense (~5.3%) integrated water vapor transport (IVT), longer duration (~21.1%) of ARs compared to the climatological mean (1980–2019) over the western U.S. AR frequency was also higher (~50.4%) in the negative AO phase than the climatological mean, but there was no statistically significant difference between either negative AO or positive AO phase, particularly in southern California.

Lastly, we also showed the linkages between the low snow water equivalent (SWE) and high low-level temperature during the positive AO phase with little connection between the AO and rain-on-snow (ROS) events. It was also shown that positive AO is related to

warmer temperature and reduced SWE, and these relationships were more statistically significant and stronger in recent years. These findings are well aligned and consistent with previous research [16,45,46], while our study further reports more recent trends focusing on the western U.S. during wet months for extended periods using long-term state-of-the-art satellite and local measurements.

While this study can offer an improved understanding of the connection between large-scale climate variability, AR characteristics, local precipitation, and snowpack, there is still a limitation. (1) Although we illustrated how IVT and precipitation could be related to the AO phase in selected periods, no clear relationship was obtained among ROS, AR, and AO during the entire period. This may be associated with the number of data sampling and the uncertainty of precipitation product. (2) We also did not consider other climate variabilities, such as the Pacific North America Oscillation (PNA), Madden-Julian Oscillation (MJO), and El Nino Southern Oscillation (ENSO), to associate AO to ARs and SWE characteristics solely. However, the interplay among climate variabilities can be possible. Indeed, a recent study showed that the spring AO and the subsequent winter ENSO are highly modulated by the phase of the preceding November AO [52]. (3) Different geographical regions and their association with AR and AO are other research areas to investigate for global and regional implications. (4) Furthermore, although there is a negative SWE–temperature–AO association over northern California at a monthly time scale, how these relationships vary at different time scales (daily or weekly and synoptic time scales) in conjunction with other dynamical and thermodynamical processes was not pursued in this study.

This study emphasizes that the synoptic conditions shaped by the different phases of climate variability, such as AO, have a different impact on the characteristics of extreme precipitation events such as ARs, and snowpack over the local region. The projection of the greater reduction in SWE under the warmer low-level atmospheric temperature and persistent high sea level pressure (SLP) and low-level tropospheric stability (LTS) in recent years may lead to more wildfire-prone conditions over the western U.S. For example, the year 2020 was the strongest positive AO year since 2000 [50] as well as the second warmest year [51] and was also reported to have record-breaking wildfire events [53]. Improved understanding of the factors controlling local precipitation and snowpack in the different phases of climate variability is crucial for securing water resources, preventing wildfire events, and ultimately protecting the whole ecosystem under a warming climate.

Author Contributions: Conceptualization: J.-M.R. and S.C.; methodology and software: S.L. and J.-M.R.; data curation and formal analysis: S.L. and J.-M.R.; writing: S.L., J.-M.R. and S.C.; visualization: S.L. and J.-M.R.; supervision, J.-M.R. and S.C.; project administration and funding acquisition, S.C. All authors have read and agreed to the published version of the manuscript.

Funding: This research was partially funded by the U.S. Department of Commerce, National Oceanic and Atmospheric Administration, Educational Partnership Program under Agreement No. NA16SEC4810006.

Institutional Review Board Statement: Not applicable.

Informed Consent Statement: Not applicable.

Data Availability Statement: The data presented in this study are openly available via the links provided in the Reference section.

Acknowledgments: The authors thank Jonathan J. Rutz for providing us with the open access AR catalog dataset through ftp://sioftp.ucsd.edu/CW3E_DataShare/Rutz_AR_Catalog (accessed on 30 June 2022). The distribution of the MERRA-2 data set is funded by NASA's Science Mission Directorate. MERRA-2 data are produced by the Global Modeling and Assimilation Office (GMAO). The IMERG data are provided by the NASA/Goddard Space Flight Center's PMM Science Team and Precipitation Processing System (PPS), which develop and compute the IMERG data as a contribution to GPM and are archived at the NASA Goddard Earth Science Data and Information System Center (GES DISC). This study was partly funded by the U.S. Department of Commerce, National

Oceanic and Atmospheric Administration, Educational Partnership Program under Agreement No. NA16SEC4810006.

Conflicts of Interest: The authors declare no conflict of interest.

References

1. Zhu, Y.; Newell, R.E. A proposed algorithm for moisture fluxes from atmospheric rivers. *Mon. Weather Rev.* **1998**, *126*, 725–735. [CrossRef]
2. Rutz, J.; Steenburgh, W.J.; Ralph, F.M. Climatological characteristics of atmospheric rivers and their inland penetration over the western United States. *Mon. Weather Rev.* **2014**, *142*, 905–921. [CrossRef]
3. Guan, B.; Waliser, D.E. Detection of atmospheric rivers: Evaluation and application of an algorithm for global studies. *J. Geophys. Res. Atmos.* **2015**, *120*, 12514–12535. [CrossRef]
4. Shields, C.A.; Rutz, J.J.; Leung, L.-Y.; Ralph, F.M.; Wehner, M.; Kawzenuk, B.; Lora, J.M.; McClenny, E.; Osborne, T.; Payne, A.E.; et al. Atmospheric river tracking method intercomparison project (ARTMIP): Project goals and experimental design. *Geosci. Model Dev.* **2018**, *11*, 2455–2474. [CrossRef]
5. Zhou, Y.; Kim, H.; Guan, B. Lifecycle of atmospheric rivers: Identification and climatological characteristics. *J. Geophys. Res. Atmos.* **2018**, *123*, 12715–12725. [CrossRef]
6. Guan, B.; Waliser, D.E. Tracking atmospheric rivers globally: Spatial distributions and temporal evolution of life cycle characteristics. *J. Geophys. Res. Atmos.* **2014**, *124*, 12523–12552. [CrossRef]
7. Ralph, F.M.; Dettinger, M.D. Storms, floods, and the science of atmospheric rivers. *Eos. Trans. AGU* **2011**, *92*, 265–266. [CrossRef]
8. Newell, R.E.; Newell, N.E.; Zhu, Y.; Scott, C. Tropospheric rivers?—A pilot study. *Geophys. Res. Lett.* **1992**, *19*, 2401–2404. [CrossRef]
9. Zhu, Y.; Newell, R.E. Atmospheric rivers and bombs. *Geophys. Res. Lett.* **1994**, *21*, 1999–2002. [CrossRef]
10. Dettinger, M.D.; Ralph, F.M.; Das, T.; Neiman, P.J.; Cayan, D.R. Atmospheric rivers, floods and the water resources of California. *Water* **2011**, *3*, 445–478. [CrossRef]
11. Ralph, F.M.; Coleman, T.; Neiman, P.J.; Zamora, R.J.; Dettinger, M.D. Observed impacts of duration and seasonality of atmospheric-river landfalls on soil moisture and runoff in coastal northern California. *J. Hydrometeorol.* **2013**, *14*, 443–459. [CrossRef]
12. Dettinger, M.D. Atmospheric rivers as drought busters on the US West Coast. *J. Hydrometeorol.* **2013**, *14*, 1721–1732. [CrossRef]
13. Guan, B.; Waliser, D.E.; Ralph, F.M.; Fetzer, E.J.; Neiman, P.J. Hydrometeorological characteristics of rain-on-snow events associated with atmospheric rivers. *Geophys. Res. Lett.* **2016**, *43*, 2964–2973. [CrossRef]
14. Goldenson, N.; Leung, L.R.; Bitz, C.M.; Blanchard-Wrigglesworth, E. Influence of atmospheric rivers on mountain snowpack in the western United States. *J. Clim.* **2018**, *31*, 9921–9940. [CrossRef]
15. Ryoo, J.-M. Coauthors Terrain trapped airflows and precipitation variability during an atmospheric river event. *J. Hydrometeorol.* **2020**, *21*, 355–375. [CrossRef]
16. Guan, B.; Molotch, N.P.; Waliser, D.E.; Fetzer, E.J.; Neiman, P.J. The 2010/2011 snow season in California's Sierra Nevada: Role of atmospheric rivers and modes of large-scale variability. *Water Resour. Res.* **2013**, *49*, 6731–6743. [CrossRef]
17. McCabe-Glynn, S.; Johnson, K.R.; Strong, C.; Zou, Y.; Yu, J.Y.; Sellars, S.; Welker, J.M. Isotopic signature of extreme precipitation events in the western U.S. and associated phases of Arctic and tropical climate modes. *J. Geophys. Res. Atmos.* **2016**, *121*, 8913–8924. [CrossRef]
18. NOAA National Centers for Environmental Information. Home/Climate Monitoring/ENSO/Technical Discussion. 2022. Available online: https://www.ncdc.noaa.gov/teleconnections/enso/technical-discussion (accessed on 2 May 2022).
19. Ryoo, J.-M.; Kaspi, Y.; Waugh, D.W.; Kiladis, G.N.; Waliser, D.E.; Fetzer, E.J.; Kim, J. Impact of Rossby wave breaking on US West Coast winter precipitation during ENSO events. *J. Clim.* **2013**, *26*, 6360–6382. [CrossRef]
20. Kamae, Y.; Mei, W.; Xie, S.P.; Naoi, M.; Ueda, H. Atmospheric rivers over the northwestern Pacific: Climatology and interannual variability. *J. Clim.* **2017**, *30*, 5605–5619. [CrossRef]
21. Matsuo, K.; Heki, K. Anomalous precipitation signatures of the Arctic Oscillation in the time-variable gravity field by GRACE. *Geophys. J. Int.* **2012**, *190*, 1495–1506. [CrossRef]
22. Kim, S.; Chiang, J.C. Atmospheric river lifecycle characteristics shaped by synoptic conditions at genesis. *Int. J. Climatol.* **2022**, *42*, 521–538. [CrossRef]
23. NASA Goddard Space Flight Center. Available online: https://gpm.nasa.gov/science/atmospheric-river-slams-california (accessed on 16 October 2021).
24. Molod, A.; Takacs, L.; Suarez, M.; Bacmeister, J. Development of the GEOS-5 atmospheric general circulation model: Evolution from MERRA to MERRA2. *Geosci. Model Dev.* **2015**, *8*, 1339–1356. [CrossRef]
25. Bosilovich, M.G.; Lucchesi, R.; Suarez, M. *MERRA-2: File Specification. GMAO Office Note No. 9*; Version 1.1; Global Modeling and Assimilation Office: Greenbelt, MD, USA, 2016; p. 73. Available online: http://gmao.gsfc.nasa.gov/pubs/office_notes (accessed on 31 July 2022).
26. Global Modeling and Assimilation Office (GMAO). *inst3_3d_asm_Cp: MERRA-2 3D IAU State, Meteorology Instantaneous 3-Hourly (p-coord, 0.625x0.5L42)*; Version 5.12.4; Goddard Space Flight Center Distributed Active Archive Center (GSFC DAAC): Greenbelt, MD, USA, 2015. [CrossRef]

27. Global Modeling and Assimilation Office (GMAO). *instM_3d_asm_Np: MERRA-2 3D IAU State, Meteorology Instantaneous 3-Dimensional Monthly Mean Data (p-coord, 0.625x0.5L42)*; Version 5.12.4; Goddard Space Flight Center Distributed Active Archive Center (GSFC DAAC): Greenbelt, MD, USA, 2015. [CrossRef]
28. Global Modeling and Assimilation Office (GMAO). *inst1_2d_int_Nx: MERRA-2 2D IAU State, Meteorology Instantaneous 2-Dimensional Monthly Mean Data (p-coord, 0.625x0.5L42)*; Version 5.12.4; Goddard Space Flight Center Distributed Active Archive Center (GSFC DAAC): Greenbelt, MD, USA, 2015. [CrossRef]
29. Collow, A.B.M.; Shields, C.A.; Guan, B.; Kim, S.; Lora, J.M.; McClenny, E.E.; Nardi, K.; Payne, A.; Reid, K.; Shearer, E.J.; et al. An overview of ARTMIP's Tier 2 Reanalysis Intercomparison: Uncertainty in the detection of atmospheric rivers and their associated precipitation. *J. Geophys. Res. Atmos.* **2022**, *127*, e2021JD036155. [CrossRef]
30. Cobb, A.; Delle Monache, L.; Cannon, F.; Ralph, F.M. Representation of dropsonde-observed atmospheric river conditions in reanalyses. *Geophys. Res. Lett.* **2021**, *48*, e2021GL093357. [CrossRef]
31. Ralph, F.M.; Rutz, J.J.; Cordeira, J.M.; Dettinger, M.D.; Anderson, M.; Reynolds, D.; Schick, L.J.; Smallcomb, C. A scale to characterize the strength and impacts of atmospheric rivers. *Bull. Am. Meteorol. Soc.* **2019**, *100*, 269–289. [CrossRef]
32. NASA EARTHDATA GPM IMERG Final Precipitation L3 1 Month 0.1 Degree × 0.1 Degree V06 (GPM_3IMERGM). 2020. Available online: https://disc.gsfc.nasa.gov/datasets/GPM_3IMERGM_06/summary?keywords=3B-HHR-L.MS.MRG.3IMERG (accessed on 7 April 2020).
33. Tapiador, F.J.; Navarro, A.; García-Ortega, E.; Merino, A.; Sánchez, J.L.; Marcos, C.; Kummerow, C. The contribution of rain gauges in the calibration of the IMERG product: Results from the first validation over Spain. *J. Hydrometeorol.* **2020**, *21*, 161–182. [CrossRef]
34. Gentilucci, M.; Pambianchi, G. Prediction of Snowmelt Days Using Binary Logistic Regression in the Umbria-Marche Apennines (Central Italy). *Water* **2022**, *14*, 1495. [CrossRef]
35. Stephens, G.L.; Vane, D.G.; Boain, R.J.; Mace, G.G.; Sassen, K.; Wang, Z.; Illingworth, A.J.; O'Connor, E.J.; Rossow, W.B.; Durden, S.L.; et al. The CloudSat mission and the A-Train: A new dimension to space-based observations of clouds and precipitation. *Bull. Am. Meteorol. Soc.* **2002**, *83*, 1771–1790. [CrossRef]
36. Naud, C.M.; Jeyaratnam, J.; Booth, J.F.; Zhao, M.; Gettelman, A. Evaluation of Modeled Precipitation in oceanic Extratropical Cyclones using IMERG. *J. Clim.* **2020**, *33*, 95–113. [CrossRef]
37. Naud, C.M.; Booth, J.F.; Lebsock, M.; Grecu, M. Observational constraint for precipitation in extratropical cyclones: Sensitivity to data sources. *J. Appl. Meteorol. Climatol.* **2018**, *57*, 991–1009. [CrossRef]
38. Tan, M.L.; Santo, H. Comparison of GPM IMERG, TMPA 3B42 and PERSIANN-CDR satellite precipitation products over Malaysia. *Atmos. Res.* **2018**, *202*, 63–76. [CrossRef]
39. Grecu, M.; Olson, W.S.; Munchak, S.J.; Ringerud, S.; Liao, L.; Haddad, Z.; Kelley, B.L.; McLaughlin, S.F. The GPM combined algorithm. *J. Atmos. Ocean. Technol.* **2016**, *33*, 2225–2245. [CrossRef]
40. Huffman, G.J.; Adler, R.F.; Morrissey, M.; Bolvin, D.T.; Curtis, S.; Joyce, R.; McGavock, B.; Susskind, J. Global precipitation at one-degree daily resolution from multisatellite observations. *J. Hydrometeorol.* **2001**, *2*, 36–50. [CrossRef]
41. NOAA National Centers for Environmental Information. Arctic Oscillation (AO). 2021. Available online: https://www.ncdc.noaa.gov/teleconnections/ao/ (accessed on 9 February 2021).
42. Department of Water Resources. CDEC Webservice JSON and CSV. 2021. Available online: https://cdec.water.ca.gov/dynamicapp/wsSensorData (accessed on 11 September 2021).
43. Scherrer, S.C. Temperature monitoring in mountain regions using reanalyses: Lessons from the Alps. *Environ. Res. Lett.* **2020**, *15*, 044005. [CrossRef]
44. Harris, S.M.; Carvalho, L.M.V. Characteristics of southern California atmospheric rivers. *Theor. Appl. Climatol.* **2018**, *132*, 965–981. [CrossRef]
45. Thompson, D.W.J.; Wallace, J.M. The Arctic oscillation signature in the wintertime geopotential height and temperature fields. *Geophys. Res. Lett.* **1998**, *25*, 1297–1300. [CrossRef]
46. Thompson, D.W.J.; Wallace, J.M. Annular Modes in the Extratropical Circulation. Part I: Month-To-Month Variability. *J. Clim.* **2000**, *13*, 1000–1016. [CrossRef]
47. Bonner, W.D. Climatology of the low-level jet. *Mon. Weather Rev.* **1968**, *96*, 833–850. [CrossRef]
48. Brill, K.F.; Uccellini, L.W.; Burkhart, R.P.; Warner, T.T.; Anthes, R.A. Numerical Simulations of a Transverse Indirect Circulation and Low-Level Jet in the Exit Region of an Upper-Level Jet. *J. Atmos. Sci.* **1985**, *42*, 1306–1320. [CrossRef]
49. Zechiel, P.R.; Chiao, S. Climate Variability of Atmospheric Rivers and Droughts over the West Coast of the United States from 2006 to 2019. *Atmosphere* **2021**, *12*, 201. [CrossRef]
50. Climate. 2021. Available online: https://www.climate.gov/news-features/understanding-climate/climate-variability-arctic-oscillation (accessed on 15 July 2022).
51. NASA. 2021. Available online: https://www.nasa.gov/press-release/2020-tied-for-warmest-year-on-record-nasa-analysis-shows (accessed on 30 July 2022).
52. Chen, S.; Chen, W.; Yu, B. Modulation of the relationship between spring AO and the subsequent winter ENSO by the preceding November AO. *Sci. Rep.* **2018**, *8*, 6943. [CrossRef] [PubMed]
53. Keeley, J.E.; Syphard, A.D. Large California Wildfires: 2020 fires in historical context. *Fire Ecol.* **2021**, *17*, 22. [CrossRef]